Surface & Coatings Technology 520 (2026) 133044

Contents lists available at ScienceDirect

Surface & Coatings Technology

journal homepage: www.elsevier.com/locate/surfcoat

Fast electrochemical deposition of corrosion resistant mixed hydroxide films from Zn/Al-nitrate aqueous electrolytes on zinc coated steel

Chen-Ni Liu [a,1,2], Lukas Ruhm [a,1], Marten Huck [b,c], Hans-Georg Steinrück [b,c], Philipp Wagener [d], Marcel Roth [e], Ingo Klüppel [e], Guido Grundmeier [a,*]

[a] Paderborn University, Technical and Macromolecular Chemistry, Warburger Straße 100, 33098, Paderborn, Germany
[b] Forschungszentrum Jülich GmbH, Institute for a Sustainable Hydrogen Economy (INW), 52428, Jülich, Germany
[c] RWTH Aachen University, Institute of Physical Chemistry, Landoltweg 2, 52074, Aachen, Germany
[d] Parker Hannifin Manufacturing GmbH & Co. KG, Am Metallwerk 9, 33659, Bielefeld, Germany
[e] Dörken Coatings GmbH & Co. KG, Wetterstraße 58, 58313, Herdecke, Germany

ARTICLE INFO

Keywords:
Mixed hydroxide films
Electrodeposition
Corrosion protection
Zinc coated steel

ABSTRACT

Corrosion resistant amorphous mixed zinc/aluminium (oxy)hydroxide films were electrodeposited on zinc coated steel from aqueous solutions containing sodium nitrate, zinc nitrate and aluminium nitrate. The ratio of Zn^{2+} and Al^{3+} in the solution was 5:2. Homogeneous films were cathodically deposited within 10 s. The resulting microstructure of the films was analyzed by means of field-emission scanning electron microscopy (FE-SEM). The film deposition rate was estimated by determination of the cross-sectional film thickness to be about 0.5 nm/s. The deposition mechanism was revealed based on the film composition, which was characterized by means of X-ray photoelectron spectroscopy (XPS), X-ray diffraction (XRD), Raman spectroscopy, and time-dependent Fourier transform infrared reflection-absorption spectroscopy (FT-IRRAS) measurements. The formation of a predominantly amorphous aluminium (oxy)hydroxide enriched film was observed. Electrochemical corrosion analysis by electrochemical impedance spectroscopy (EIS) and linear sweep voltammetry (LSV) showed that the deposited films led to a significant inhibition of both cathodic and anodic corrosion reactions already at deposition time of 10 s corresponding to a film thickness of about 5 nm.

1. Introduction

The corrosion resistance of galvanized steels can be significantly improved by suitable conversion coatings [1]. The purpose of the surface chemical conversion of the zinc coating is the creation of an additional electrochemical barrier supplementing the active corrosion protection provided by the zinc coating itself [1]. This type of additional protection by passivation can for instance be achieved by aluminium-containing conversion coatings [2–5]. The majority of approaches for such coatings are based on the formation of layered double hydroxides (LDH) [4–6]. However, the preparation of LDH conversion coatings usually requires unfavorable long immersion times and high bath temperatures [6,7]. The possible application of other aluminium (oxy)hydroxide coatings for the corrosion protection of zinc coated steel has scarcely been investigated so far [8]. Multiple approaches exist for the preparation of aluminium oxide-based barrier films. However, most of them are based on physical vapor deposition (PVD) [9–11], chemical vapor deposition (CVD) [2,12] or sol-gel techniques [13].

Electrochemically supported depositions may be a suitable alternative to harness the use of aluminium oxide-based coatings for corrosion protection, as electrodeposition is a fast and efficient method to prepare homogeneous coatings even on demanding surfaces. However, this approach has rarely been used for the deposition of aluminium oxides [14–16]. Haleem et al. report the cathodic electrodeposition of aluminium oxide in solutions containing aluminium sulfate and sodium thiosulfate, but did not investigate their corrosion inhibition [15]. Watkins et al. report an aluminium oxide layer based on electrodeposition using organic aluminium salts along with significant corrosion inhibition [16].

Mixed zinc and aluminium nitrate solutions are usually employed for

* Corresponding author.
E-mail address: guido.grundmeier@uni-paderborn.de (G. Grundmeier).
[1] These authors contributed equally to this work and share first authorship.
[2] Present address: Verwaltungs-Berufsgenossenschaft (VBG), Bezirksverwaltung Bielefeld, Nikolaus-Dürkopp-Straße 8, 33602, Bielefeld, Germany.

https://doi.org/10.1016/j.surfcoat.2025.133044
Received 25 July 2025; Received in revised form 26 September 2025; Accepted 4 December 2025
Available online 8 December 2025

the cathodic electrodeposition of aluminium doped zinc oxide (AZO) [17,18] and ZnAl-LDH [4,19,20]. Tseng et al. investigated the influence of the aluminium nitrate concentration on the electrodeposition of AZO on a zinc oxide coated substrate, revealing the formation of a mixed amorphous film for Zn:Al ratios lower than 8, while at higher ratios AZO nanorods were deposited [17]. The electrodeposition of ZnAl-LDH was investigated by Yarger et al. revealing a strong dependence of the deposited phases on the potential and pH of the aqueous nitrate solution [20]. They further hypothesize that elevated temperatures lead to increased formation of byproducts [20] based on a study by Otani et al. on the temperature dependence of zinc oxide electrodepositions [21]. Packter et al. investigated the pH dependence of the coprecipitation of zinc and aluminium hydroxides in aqueous nitrate solutions revealing that aluminium hydroxides start to precipitate at a lower pH (4.5) compared to zinc hydroxides (7.2), whereas coprecipitation starts at pH 5.5 [22].

The deposition of zinc/aluminium hydroxide films on zinc coated steel has recently shown promising results regarding an application as conversion coatings for corrosion protection [23–26]. Xu et al. [26] successfully deposited a ZnAl-LDH conversion coating on galvanized steel within 300 s by electrodeposition. Yasakau et al. [25] deposited a ZnAl-LDH coating on a zinc substrate by hydrothermal growth for 20 h.

We here present the fast electrodeposition of amorphous mixed hydroxide films on zinc coated steel from aqueous electrolytes containing nitrates. Thereby the films grown from an electrolyte consisting of basic chemicals are homogeneous, as shown by field-emission scanning electron microscopy (FE-SEM) and energy-dispersive X-ray spectroscopy (EDX) imaging. Electrochemical measurements showed promising results regarding the application of the coating as a temporary corrosion protection or as a conversion layer for organic sealings.

2. Materials and methods

2.1. Chemicals and materials

All chemicals were used without further purification. Zinc nitrate hexahydrate (extra pure) and sodium nitrate (99 %) were purchased from Arcos ORGANICS, Spain. Aluminium nitrate nonahydrate, boric acid, sodium sulfate, sodium chloride, and sodium borate decahydrate were purchased in Reag. Ph Eur. grade from Merck KGaA (Germany). Purified water was received by use of water system SG Ultra Clear UV plus (Evoqua Water Technologies, Germany).

Zinc coated steel (Dörken Coatings GmbH & Co. KG, Germany) was chosen as substrate. The zinc coating was electrodeposited (−15.8 mA/cm^2, 45 min) from an alkaline solution with a zinc concentration of 15 g/L and 150 g/L NaOH. The zinc coating had an approximate thickness of 3.7 μm. The sheet metal was immersed in 1 % HNO_3 for 20 s, washed with purified water and blown dry in a purified airstream as a pretreatment.

2.2. Deposition process

Deposition was performed in an aqueous electrolyte consisting of 0.01 M $Zn(NO_3)_2$, 0.004 M $Al(NO_3)_3$ and 0.1 M $NaNO_3$ with a pH of 4.05. For deposition, the electrolyte was heated to 60 °C and a current density of −0.15 mA/cm^2 was applied. The experimental parameters were chosen and optimized starting from common parameters for the electrodeposition of nanocrystalline zinc oxide and LDH films. Deposition time was varied from 10 to 300 s. Specimens are referred to their deposition times, e.g., ED_{10} is the specimen obtained after 10 s of electrodeposition. Samples were thoroughly rinsed with purified water and dried using purified air after the deposition.

2.3. Characterization

The film morphologies were investigated by means of FE-SEM and EDX using a NEON 40 (Carl Zeiss SMT AG, Germany) equipped with a focused ion beam (FIB) and an UltraDry EDX detector (Thermo Fisher Scientific Inc., USA). Cross-section images were recorded at a tilt angle of 36°. The layer thickness was approximated from one cross-section using the integrated tilt correction of the Zeiss software. EDX imaging was performed with a low acceleration voltage (5 kV) to increase the surface sensitivity.

The adhesion of the electrodeposited coating was examined by means of a tape test. An aluminium tape (Optima Tape Sp. z o.o., Poland) was applied at room temperature using a 2 kg rubber roller that was moved over the surface five times. The relative humidity was 36 % and the tape was removed using an angle of 180° after 1 min of attachment. The surfaces were examined by FE-SEM before and after the test to identify the fracture mode.

Fourier transform infrared reflection-absorption spectroscopy (FT-IRRAS) measurements were performed by means of a spectrometer Vertex 70 (Bruker Corporation, USA) at an angle of incidence of 72° with a resolution of 4 cm^{-1}. For each spectrum 256 single spectra were recorded and averaged. For referencing a clean gold substrate was used. For evaluation on-board software OPUS 7 was used.

For Raman spectroscopic investigations a dispersive spectrometer In-Via (Renishaw, UK) was used. Excitation was conducted by a RL633 nm HeNe laser and a 50× objective resulting in a power density of 5.8 mW/μm^2.

X-ray diffraction (XRD) measurements were performed in grazing incidence geometry (GIXRD) using a Bruker D8 DiscoverPlus multipurpose diffractometer system. A copper source (λ = 1.5406 Å) was utilized with a Goebel mirror focusing optic, a Ni k_β-filter, a 0.1 mm slit and a scatter guard on the primary beam path. The secondary beam path consisted of 0.3° equatorial soller slits and a 300 × 300 px 0D detector (EIGER2 R 500 k). The measurements were performed at an incidence angle of 0.6° between 20 and 80° 2θ, with a step size of 0.025° and a counting time of 20 s per data point.

For X-ray photoelectron spectroscopy (XPS) measurements an ESCA+ system (Omicron NanoTechnology GmbH, Germany) equipped with a hemispherical energy analyzer was used. The base pressure was $<5 \times 10^{-10}$ mbar and the analyzer pass energy was 100 eV for survey and 20 eV for element spectra. Photoelectron excitation was conducted by a monochromated Al K_α (1486.7 eV) X-ray source (Omicron XM 1000) with a spot diameter of 600 μm. The take-off angle of detected photoelectrons was set to 60° with respect to the plane of the probed surface. Neutralization was performed with an electron flood gun. The C 1s peak of adventitious carbon was set to a binding energy of 284.6 eV as an internal reference. Data evaluation was performed by means of software Casa-XPS (Casa Software Ltd., Japan). For peak fitting, combinations of Gaussian and Lorentzian distributions and Shirley backgrounds were used.

Electrochemical measurements were performed by means of a Reference 3000 potentiostat (Gamry Instruments, USA) in a custom designed cell at room temperature. Electrodes were arranged in classical three electrode set-up, with a Pt-wire as counter electrode, an Ag/AgCl electrode (sat. KCl) as reference electrode and the probed specimen as working electrode. The probed area was 0.785 cm^2. A borate buffer (pH ~ 8.3) with addition of NaCl was chosen as the electrolyte for electrochemical corrosion studies. The electrolyte consisted of 0.2 mol/L boric acid, 0.05 mol/L sodium sulfate, 0.05 mol/L sodium tetraborate and 0.05 mol/L sodium chloride. After equilibrium time of 400 s the measurements were started. Electrochemical impedance spectroscopy (EIS) measurements in potentiostatic mode were conducted in the range of 100,000–0.1 Hz. Thereby AC voltage was set 10 mV rms and DC voltage was set 0 V with respect to open circuit potential. Linear sweep voltammetry (LSV) was performed in the range of −0.3 to +0.8 V vs. open circuit potential. The scan rate was set to 0.5 mV/s, and the step size was 0.5 mV. Corrosion current densities (i_{corr}) and potentials (E_{corr}) were obtained from the LSV measurements by Tafel slope extrapolation using the Gamry *E*-Chem analyst software. The results of two measurements

were averaged for each deposition time.

An estimation of the interfacial pH during the electrodeposition at 60 °C was calculated using COMSOL Multiphysics 5.6 (COMSOL AB, Sweden). The pH was approximated based on the assumption that one OH^- is generated at the electrode surface per transferred electron during the galvanostatic deposition. The transport of H_3O^+ and OH^- was assumed to be exclusively diffusive. In addition, the autoprotolysis of water and recombination of H^+/OH^- was taken into account based on kinetic constants as shown by Murer et al. [27]. Bulk concentrations were assumed at 2 mm distance to the electrode. The transport, hydrolysis and precipitation of Zn^{2+}/Al^{3+} were not considered for the approximation.

3. Results

3.1. Galvanostatic deposition

The time-depending development of the electrode potential during galvanostatic deposition (−0.15 mA/cm^2) was monitored (see Fig. 1). At the beginning, the potential has a value between −0.64 and −0.62 V_{SHE}. While the slope of the curves is very steep at the beginning, it flattens more at prolonged deposition time. No steady state was reached within the maximum deposition time of 300 s.

The curves encode the kinetics of the deposition process and resemble typical galvanostatic ZnO depositions [28,29]. At the beginning, the potential of the galvanostatic process shifts negatively as the nitrate reduction starts most probably due to the depletion of nitrate at the interfaces. However, after reaching a potential of about −0.64 V_{SHE} after a few seconds the film formation leads to a positive shift of the potential [28–30]. After 300 s, a potential of −0.5 V_{SHE} is reached.

This trend leads to the hypothesis that the formed surface layer allows an electron transfer to the nitrate ions not only in remaining pores but across the electrolyte/film interface [29,31]. This could be explained by the formation of ZnO as part of the deposited film.

3.2. Characterization of film morphology

FE-SEM micrographs of the surface of all specimens and the bare zinc coated substrate are shown in Fig. 2A–F. In comparison to the bare substrate (Fig. 2A) after 10 s of electrodeposition the surface of the substrate is already homogeneously coated with a porous film (Fig. 2B). The deposited films show a nanogranular structure. This morphology does not change significantly with deposition times of 30 s, 60 s 120 s and 300 s (see Fig. 2C–F).

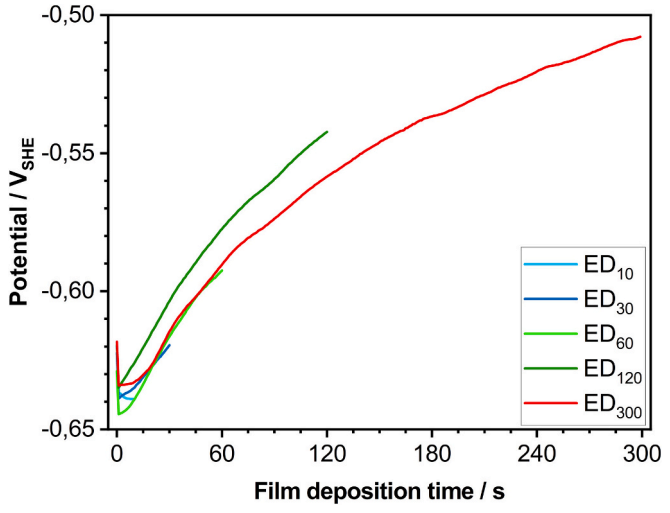

Fig. 1. Time-dependent development of the potential during galvanostatic deposition (−0.15 mA/cm^2) for different film deposition times. The indices indicate the total time of electrodeposition of the samples.

The FE-SEM images indicate the existence of nanoscopic pores, however, on a mesoscopic and macroscopic scale the films are very homogeneous already at short deposition times. Complementary to the top-view analysis, Fig. 3 shows the FE-SEM micrograph of a FIB cross section of film ED_{300}. After 300 s of deposition the film has a thickness of about 60–230 nm. This leads to a deposition rate of about 0.5 nm/s, which is within the expected range of coatings deposited from zinc and aluminium nitrate solutions by hydrothermal- or electrodeposition [18,28,30,32–35]. The adhesion of the coating on the zinc coated steel substrate was tested by application and removal of an adhesive tape (Supplementary material, Fig. S1). Fracture mainly occurred within the adhesive and at the adhesive/ED_{300} interface, indicating strong adhesion of deposited films.

3.3. Spectroscopic analysis

Analysis of chemical composition and microstructure was conducted by means of Raman spectroscopy, XRD, FT-IRRAS, EDX and XPS.

The resulting Raman spectra of deposited films after varying film deposition times are shown in Fig. 4. All spectra exhibit a single peak at 560 cm^{-1} which gets more pronounced after a deposition time of 60 s (specimen ED_{60}). This peak indicates the presence of disordered nanocrystalline ZnO [36–38]. As the signal is increasing with deposition time, the formation of ZnO is clearly part of the deposition mechanism, which is in accordance with the following XRD investigation. The absence of signals at 496 cm^{-1} (M-OH EgT) and 1080 cm^{-1} (ν_1 NO_3^-) indicates that no ZnAl-LDH-NO_3 phases are present in the film [39–41].

FT-IRRAS data of the films and an additional deposition time-dependent evaluation of selected peaks are shown in Fig. 5, the assignments of the peaks are listed in Table 1. The spectrum of the substrate shows only weak signals of water and hydroxyl-groups in the 3700–3000 cm^{-1} regime [42] and a peak sequence in the 2960–2850 cm^{-1} regime specific for CH_2/CH_3-groups due to aliphatic contaminations, which appears in all spectra. The spectrum of ED_{10} also shows a broad peak of water/hydroxyl groups, but in this case, it is more pronounced. Additionally, new peaks are visible in the fingerprint region, namely at 1630 cm^{-1}, 1500–1200 cm^{-1} and 1090–960 cm^{-1} indicating presence of water/hydroxides [43,44], carbonates/nitrates [45,46] and zinc/aluminium hydroxides/oxides [43,44,47], respectively. While the spectrum of ED_{30} is similar to ED_{10}, the spectra of ED_{60} and ED_{120} show an additional band at 730 cm^{-1} which also indicates the presence of Al—O [44,48]. The spectrum of ED_{300} shows another band at 1084 cm^{-1} which could be assigned to (pseudo) boehmite [44] or zinc hydroxide [47].

Quantification of peak integrals in the time dependent IR spectra allowed qualitative statements to be made about the development of the layer as a function of the deposition time. The evaluation of the OH-peak at ~3500 cm^{-1} by peak integration (Fig. 5) revealed a stepwise increase of the detectable number of OH-groups. During the first 10 s of deposition, the integral rapidly increases, probably due to the beginning nucleation of hydroxides on the surface, which is in agreement with the transient of the potential during the galvanostatic deposition. Afterwards, the increase of the integral is almost linear, indicating a relatively constant growth of the layer. In combination with the continuously decreasing cathodic overpotential, this indicates that the nitrate reduction takes place in existing nanopores enabling a homogeneous increase of the pH within the interfacial electrolyte and thereby a continuous deposition of the mixed hydroxide layer.

Evaluation of the metal oxide/hydroxide related band at 1020 cm^{-1} revealed an almost identical trend. This may show that the composition of the layer remains approximately constant during the deposition, as the ratio of oxides and (oxy)hydroxides does not change. However, as already discussed, the outline of the metal oxide/hydroxide band changed for ED_{300}, which could indicate an increased formation of (pseudo) boehmite and/or zinc hydroxide. Due to the high number of

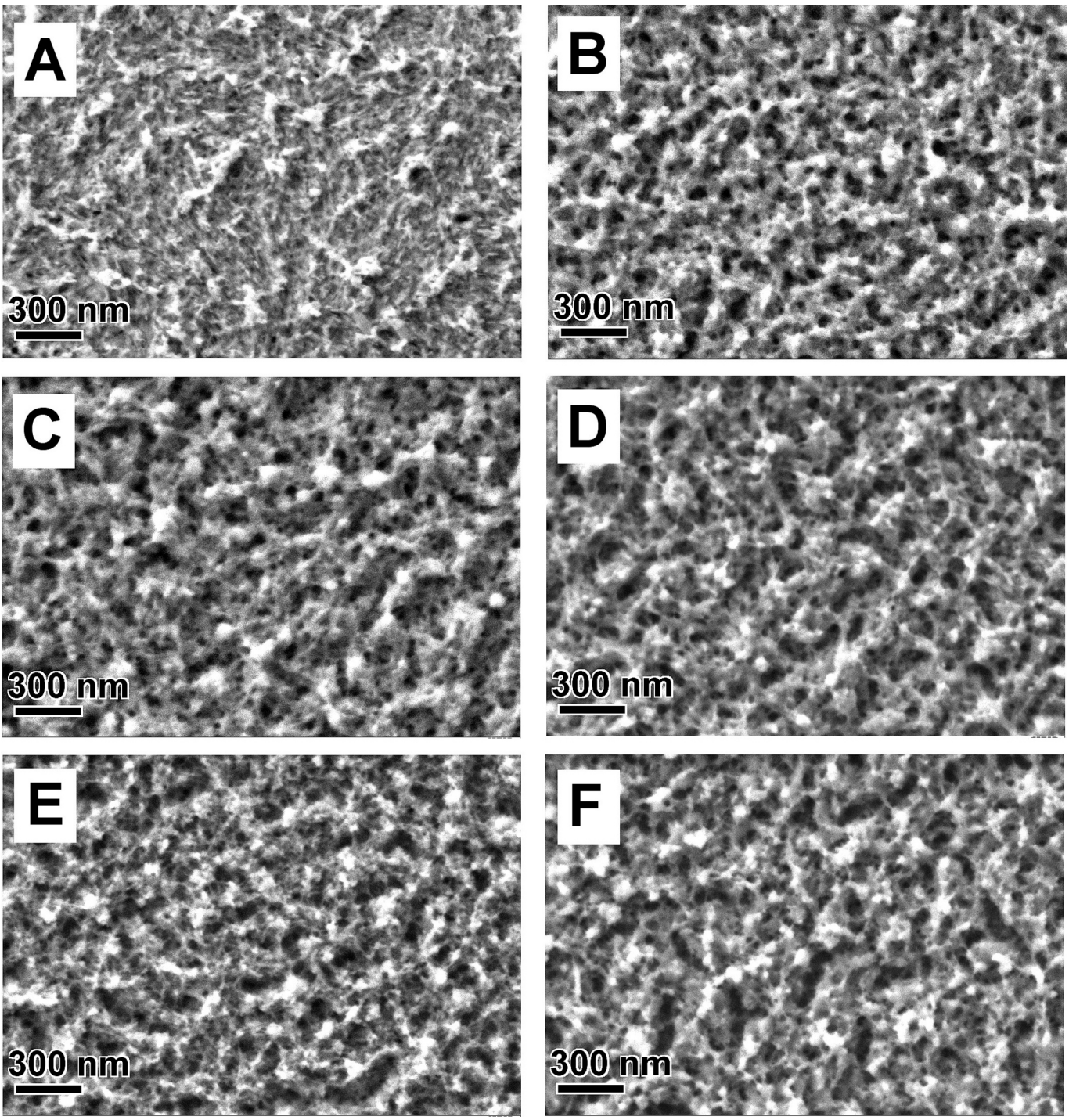

Fig. 2. (A–F): FE-SEM micrographs of surface; (A) bare zinc coated steel substrate, (B) ED_{10}, (C) ED_{30}, (D) ED_{60}, (E) ED_{120} and (F) ED_{300}.

possible components in this spectral region, further assessment of the composition based on FT-IRRAS measurements was not possible.

Fig. 6 shows XPS survey spectra of bare zinc coated steel, and the mixed hydroxide film deposited for 300 s (ED_{300}). The atomic composition of the specimens obtained from survey spectra are listed in Table 2. The survey spectrum of the substrate revealed the presence of oxygen, carbon, and zinc, which is expected due to the application of zinc coated steel. Deposition of the mixed hydroxide coating is evident from the additional signals of aluminium and nitrogen for ED_{300}. The small nitrogen contribution is most likely caused by the presence of residual nitrate/nitrite in the coating.

The results show that zinc and aluminium are both incorporated in the mixed hydroxide film during the electrodeposition process. The quantification of the measurements revealed a Zn:Al ratio of 1:4 in the ED_{300} film which shows that aluminium ions are preferentially incorporated in the surface film. The EDX analysis (Fig. S2) indicated a homogenous distribution of the two elements across the surface.

C 1s and O 1s high-resolution spectra of the substrate and ED_{300} are shown in Fig. 7. The corresponding ratios of oxygen and carbon species are listed in Table 3. The C 1s element spectra of the substrate and ED_{300} were fitted following a procedure described by Payne et al. for adventitious carbon on chromium oxide surfaces [51]. Five components at binding energies 284.6 eV (C—C), 286.1 eV (C—O), 287.3 eV (C=O), 288.5 eV (COO) and 289.5 eV (CO_3^{2-}) were fitted accordingly.

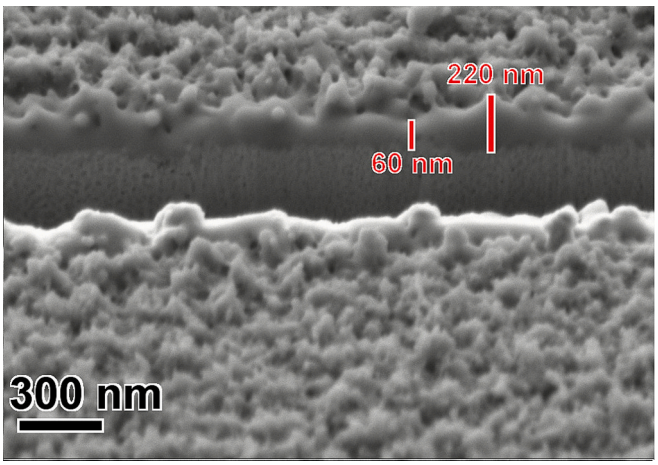

Fig. 3. SEM micrograph of cross-section of ED_{300} obtained by FIB-cut.

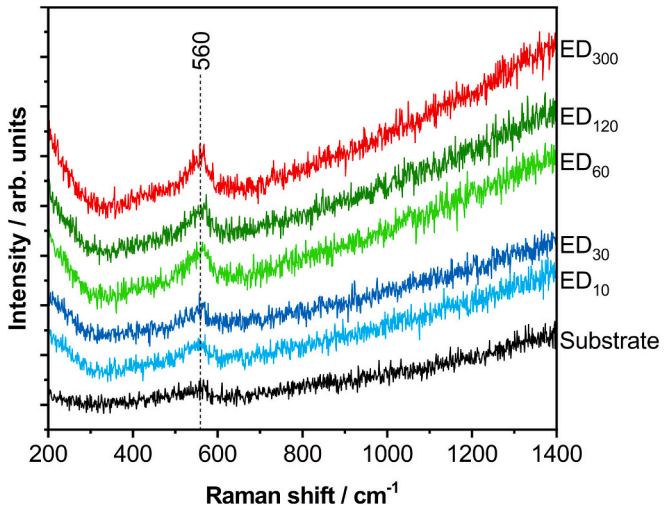

Fig. 4. Raman spectra of the bare zinc coated steel substrate and film coated specimens. The wavelength of the excitation laser was 630 nm.

Fitting of the O 1 s spectrum of the bare zinc coating was done using two components at 529.8 and 531.5 eV corresponding to the contributions of zinc oxide and hydroxide/carbonate/organic oxygen respectively [52,53]. As the contributions of hydroxides and carbonates could not be meaningfully secluded by the O 1s fitting, the percentages of carbonate and organic oxygen were determined based on the C 1s fitting. The percentage of hydroxide was in turn determined by subtraction of the contribution of carbon-bound oxygen atoms from the O 1 s signal. Thereby, an approximate passive film composition of 19 % zinc carbonate, 16 % zinc hydroxide and 65 % zinc oxide was found. The Zn:O atomic ratio of 1:1 (without organic oxygen but including carbonate) on the other hand indicated pure ZnO. However, the positions of zinc related peaks (Zn $2p_{3/2}$ 1021.3 eV) suggested the presence of metallic zinc [53], as the oxide layer is thinner than the depth of the XPS measurement, whereby the high percentage of zinc can be explained. Overall, the quantification of zinc hydroxide by XPS must be considered with caution, as Durchoslav et al. reported radiation induced accelerated transformation to zinc oxide using standard XPS parameters [54].

The O 1s spectrum of the film ED_{300} was fitted by the same

Table 1
Assignments of relevant peaks of FT-IRRAS spectra.

Peak position (cm^{-1})	Assigned group/ species	Assigned vibrations	Peak position (cm^{-1}) assigned in literature
3700–3000	Water, hydroxyl	ν(OH)	3700–3000 [42,43]
3000–2850	CH_2, CH_3	ν (CH)	3000–2850 [49]
1630	Water	ν (OH)	1680–1600 [42]
1505	Carbonate	ν $(CO_3)^{2-}$	1505 [50]
1410	Carbonate	ν $(CO_3)^{2-}$	1400 [42]
1360	Carbonate, Nitrate	ν $(CO_3)^{2-}$	1350 [42,46]
1084	(Pseudo) Boehmite	δ(OH)	1080/1090 [43,44,49]
	Zinc hydroxide		1086/1039 [47]
1020	Gibbsite/Bayerite	δ(OH)	1020 [44]
960	Al-O	ν (Al—O)	950/970 [43,44]
730	Al-O	ν (Al—O)	740 [44]

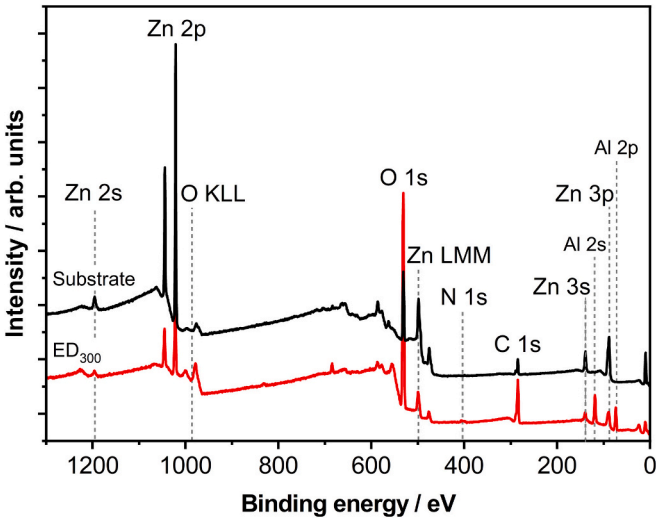

Fig. 6. XPS survey spectra of the bare zinc coated steel substrates, and the mixed hydroxide film deposited for 300 s (ED_{300}).

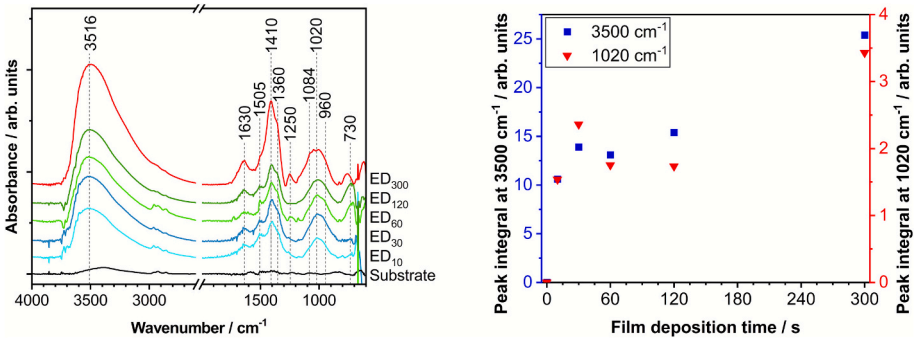

Fig. 5. Left: FT-IRRAS data of the bare zinc coated steel substrate and film coated specimens. A clean gold mirror was used as reference. Right: Evaluation of the OH-stretching regime at ~3500 cm^{-1} and the metal oxide/hydroxide regime at ~1020 cm^{-1} as a function of the deposition time.

Table 2
Elemental composition of zinc coated steel substrate and ED_{300} gained by the analysis of XPS survey spectra. Indicated errors are standard deviations of the intensity calculations by CASA XPS.

	C 1s (at.%)	O 1s (at.%)	Zn 3s (at.%)	Al 2s (at.%)
Substrate	22.5 ± 0.4	43.3 ± 0.4	34.2 ± 0.4	–
ED_{300}	25.3 ± 0.2	47.2 ± 0.2	5.6 ± 0.2	21.9 ± 0.2

procedure, but due to the high number of possible contributing zinc/aluminium species, many possible components were combined in a single peak, wherefore the resulting quantification should be considered with caution. However, the peak position of 531.5 eV indicates a mixed (oxy)hydroxide film [52,55,56]. The ratio of oxygen to the sum of zinc and aluminium (O:M) including carbonate and organic contributions was approximately 1.45. This low ratio indicates that the film consists of a considerable amount of zinc/aluminium oxide in addition to the hydroxides already confirmed by FT-IRRAS measurements. The Al 2p peak of ED_{300} (Fig. S3) is therefore most likely a superposition of aluminium oxide and (oxy)hydroxide contributions. However, the corresponding signals could not be secluded due to their small binding energy shifts [55,56].

The Zn $2p_{3/2}$ spectrum of the bare zinc coated steel shown in Fig. S4 indicates the superposition of contributions from Zn(0) and Zn(II) [53]. The corresponding Zn LMM auger peaks clearly show both contributions [57]. The modified Auger parameter was calculated as reported by Gaarenstroom and Winograd [58] and the resulting parameter of 2009.7 eV indicates the presence of zinc carbonate and/or hydrozincite [45]. However, the differentiation between Zn species is difficult, as their Auger parameters are close and measurements may be affected by radiation induced transformations [45,54]. The Zn $2p_{3/2}$ peak of ED_{300} is shifted compared to the substrate due to the absence of Zn(0). The Auger parameter is 2009.4 eV, which is a shift towards values reported for zinc hydroxide [45]. Taking the Raman measurements into account, we assume that $ZnO/Zn(OH)_2$ phases are both part of the growing film.

The grazing incidence XRD measurements shown in Fig. S5 reveal the expected presence of zinc and zinc oxide for the zinc coated steel substrate and ED_{300}. The zinc coated steel shows two additional unidentified peaks at 38.3° and 44.6°. No contributions of aluminium oxides, −hydroxides or layered double hydroxides were found. Therefore, we posit that the aluminium oxide and zinc/aluminium hydroxide phases identified in the previous spectroscopic analysis are most likely amorphous. Since the XRD measurements of the bare substrate and ED_{300} both show weak ZnO signals, it is unlikely that the absence of crystalline Al phases is due to a detection limit. The XRD results are thus consistent with the prepared films mostly consisting of amorphous aluminium (oxy)hydroxides with minor contributions of crystalline zinc oxide.

Overall, XRD, FT-IRRAS, Raman and XPS showed the presence of

Table 3
Concentrations of oxygen and carbon species in different oxidation states gained from peak fitting of O1s and C1s XPS spectra of the bare substrate and the film deposited at 300 s.

	C 1s					O 1s	
	C-C (at. %)	C-O (at. %)	C=O (at. %)	COO (at. %)	CO_3^{2-} (at.%)	Oxide (at.%)	OH/ CO_3^{2-} /Org. O (at.%)
Substrate	63.5	13.6	1.5	11.3	10.1	40.8	59.2
ED_{300}	72.8	11.0	2.6	8.7	4.9	14.7	85.3

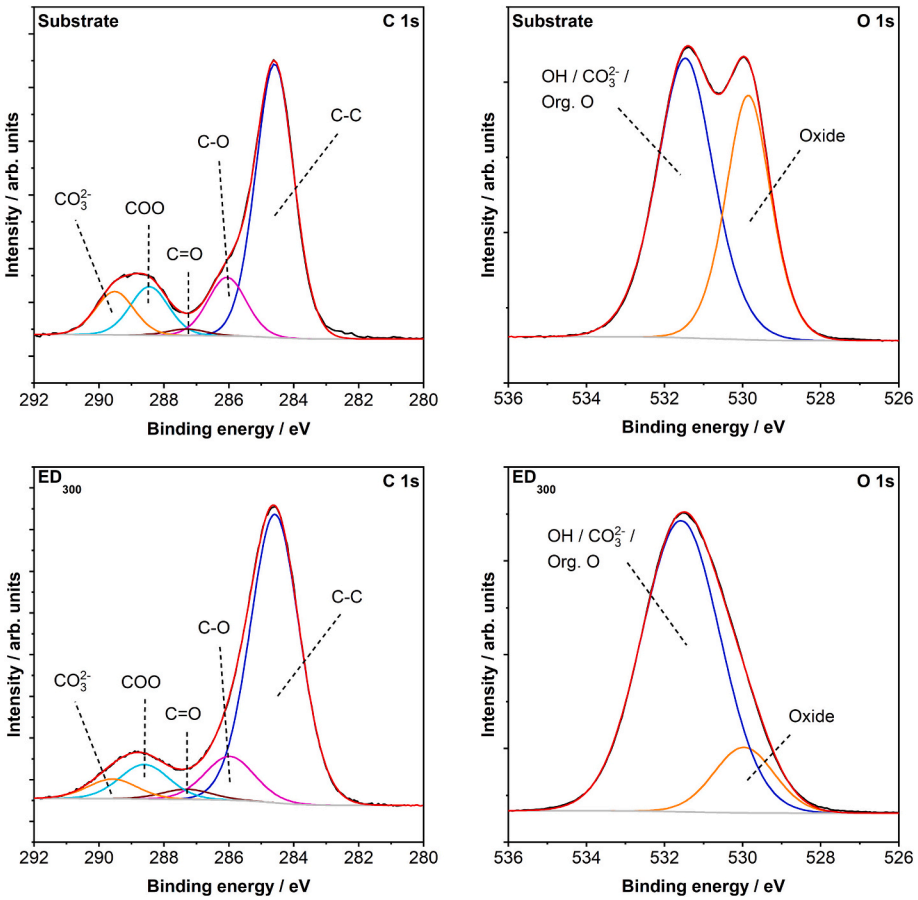

Fig. 7. XPS C 1s and O 1s core level measurements of bare zinc coated steel (Substrate) and after 300 s electrodeposition (ED_{300}).

zinc oxide, zinc hydroxide, aluminium (oxy)hydroxide, and zinc/aluminium carbonates. Aluminium is preferentially incorporated in the electrodeposited film. Furthermore, FT-IRRAS measurements indicated that the percentage of aluminium oxy(hydroxide) or zinc hydroxide may increase with deposition time.

3.4. Electrochemical corrosion analysis

Electrochemical impedance (EIS) measurements were conducted over 24 h of immersion in borate buffer. Bode plots of time-dependent EIS measurements of the specimens are depicted in Fig. 8. An additional plot of the impedance values in the pore region at 0.1 Hz versus time is shown in Fig. 9. It is visible that the deposition of the mixed hydroxide layer strongly affects the electrochemical properties of the specimens, since the minimum of the phase of ED_{10} differs from the bare substrate (Fig. 8). The phase angles for specimens with increased film thickness show two minima instead of one minimum at small immersion times. With prolonged immersion time two minima were only observed in the phase of ED_{120} and ED_{300} (Figs. S6 and 8). The corresponding impedance values at 0.1 Hz show that all films provide corrosion protection of the zinc coating as displayed in Fig. 9B. In agreement with the phase analysis, the thicker films (ED_{120} and ED_{300}) lead to the largest impedance values over the complete time of immersion. The achieved lowering of the corrosion activity based on EIS analysis can be estimated to be more than one order of magnitude as the impedance at 0.1 Hz for the bare substrate is ~6.7 kΩcm^2 and the corresponding impedance of ED_{300} is 94.2 kΩcm^2 after 24 h of immersion, respectively. The mixed hydroxide films thereby clearly act as an electrochemical barrier. Bode plots of ED_{300} and the zinc coated steel were additionally fitted (Figs. S7 and S8), whereby a significantly increased charge transfer resistance was confirmed. The electrodeposited film can be fitted using a typical model for porous coatings (Fig. S7). The Bode plots of films with lower deposition time clearly show the presence of a similar coating. However, the coatings are not stable at longer immersion in the chloride containing solution. Therefore, the impedances at lower and medium frequencies decrease, showing reduced corrosion inhibition and breakdown of the barrier film, respectively. The additional phase minima disappear accordingly, and the surfaces approach the behavior of the zinc coated steel. The coating deposited for 300 s on the other hand shows continuously increasing impedances and stronger manifestation of the second phase minimum. The results indicate that, despite its porosity, the layer formed within 300 s provides significant protection in the chloride solution within the 24 h measurement period. In addition, further passivation is evident, presumably due to corrosion products formed within the porous layer.

Complementary potentiodynamic polarization measurements were conducted. The results are shown in Fig. 10 as time-dependent Tafel-plots. Calculated Tafel-parameters are listed in Table 4. The corrosion potential (E_{corr}) of the bare zinc coated steel is at −0.9 V_{SHE}. The deposition of the mixed oxyhydroxide layer leads to an anodic shift of the corrosion potentials indicating the inhibition of metal dissolution. Parallel to the anodic shift of the corrosion potential, the corrosion current density (i_{corr}) decreases with the film thickness. It is noticeable that i_{corr} of ED_{300} is about two orders of magnitude lower than i_{corr} of the substrate which is in reasonable agreement with the EIS data. The bare zinc coated steel shows noticeable passivation, which can be expected due to the formation of zinc hydroxides at the pH of the borate buffer. However, the condition is not stable due to the presence of chlorides. Similar behavior was observed in the time-dependent Bode-plots. The electrodeposited coatings do not show additional passivation by hydroxide formation and clear signs of pitting corrosion at sufficiently anodic potentials, which is expected in chloride solutions. For the 300 s electrodeposition, the potential of the breakthrough is clearly shifted, and the current is significantly reduced compared to the shorter deposition times. The results are in good agreement with the stability of ED_{300} in the impedance experiment. Overall, the potentiodynamic measurements show significant inhibition of cathodic oxygen reduction and anodic zinc dissolution by the deposited films.

4. Discussion

The mixed hydroxide film is deposited by a precipitation-transformation mechanism as sketched in Fig. 11. By the increase of the pH due to the reduction of nitrate (Eq. (1)), zinc and aluminium (oxy)hydroxides precipitate at the interface (Eqs. (2)–(4)) [17,59,60]. In principle, these conditions can result in the formation of ZnAl-LDH coatings [19]. However, the formation of LDH strongly depends on many factors, including the pH and the ratio of the cations [7]. In our case, XRD measurements indicated that no crystalline LDH phase was formed, which may result from low pH due to the comparatively low current density of the experiment. Additionally, the films were not aged/calcinated after their deposition. An approximation of the development of the interfacial pH based on the galvanostatic nitrate reduction can be found in Fig. S9. Due to the rapid hydroxide formation at the electrode

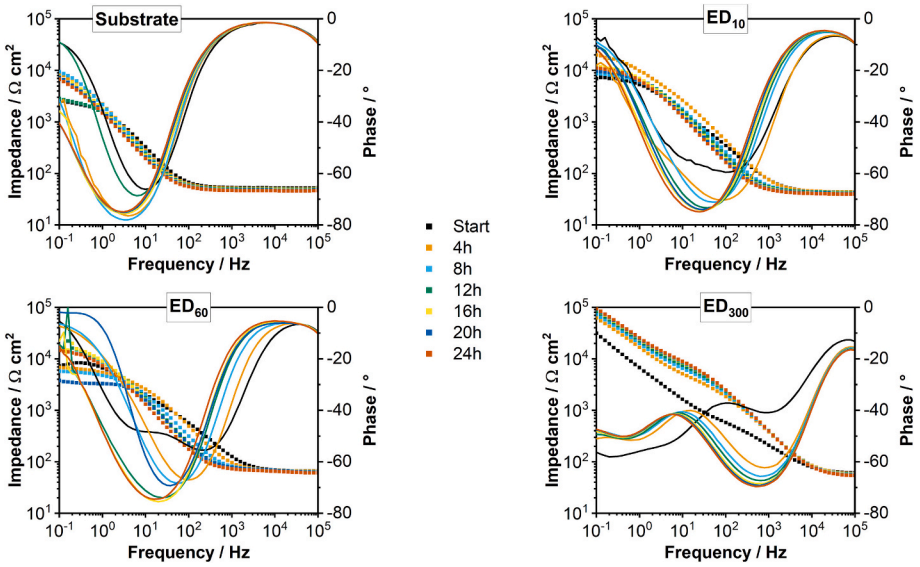

Fig. 8. Bode plots of electrochemical impedance spectroscopy measurements of specimens immersed in borate buffer at pH = 8.3 with addition of 0.05 M NaCl.

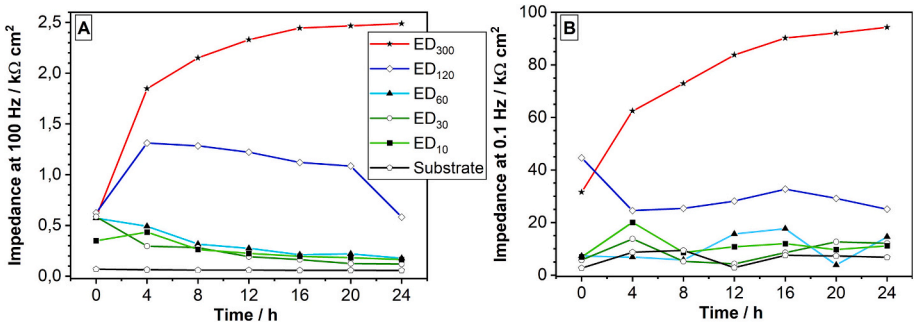

Fig. 9. (A, B): Time-dependent evolution of the impedance extracted from electrochemical impedance measurements in borate buffer at pH = 8.3 with addition of 0.05 M NaCl. (A) Impedance values at 100 Hz and (B) Impedance values at 0.1 Hz.

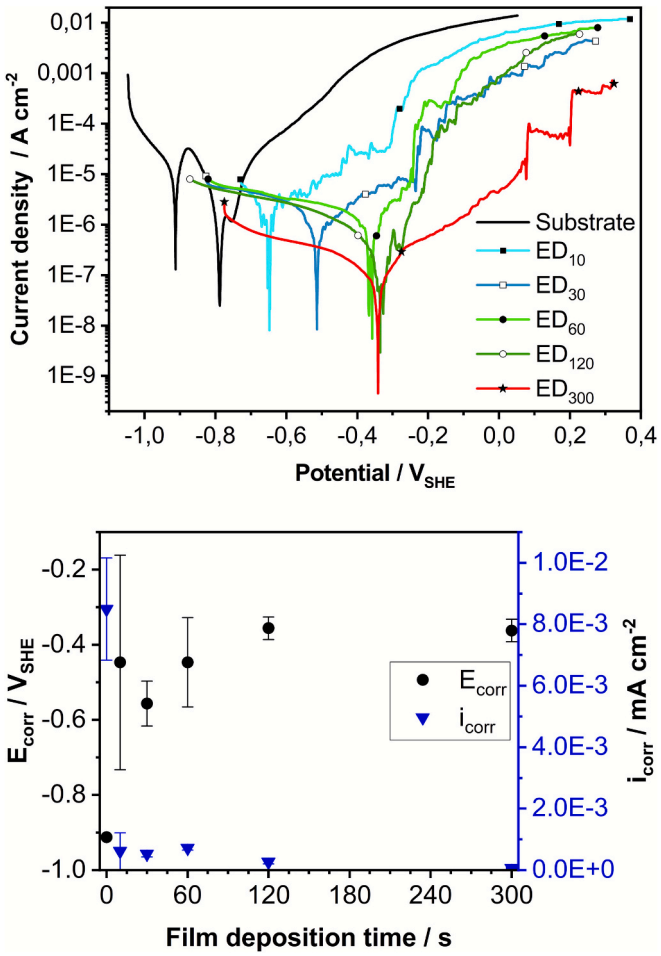

Fig. 10. Top: Potentiodynamic analysis of film coated specimen recorded in borate buffer (pH ~ 8.3) with addition of 0.05 M NaCl in comparison to the bare zinc coated steel substrate. Bottom: Corrosion current density i_{corr} and corrosion potential E_{corr} determined by potentiodynamic analysis as a function of the film deposition time.

surface, the interfacial pH rises to 11 within 30 s. The actual interfacial pH during the experiment is expected to be lower because of the beginning deposition of zinc and aluminium hydroxides.

$$NO_3^- + H_2O + 2\,e^- \rightarrow NO_2^- + 2\,OH^- \quad (1)$$

$$Zn^{2+} + 2\,OH^- \rightarrow Zn(OH)_2 \quad (2)$$

$$Al^{3+} + 3\,OH^- \rightarrow Al(OH)_3 \quad (3)$$

Table 4
Tafel-fit parameters of polarization tests conducted in borate buffer (pH = 8.3) with addition of 0.05 M NaCl.

	E_{corr} (V_{SHE})	i_{corr} (μA/cm²)	b_c (mV/dec)	b_a (mV/dec)
Bare Zn-coated steel	−0.913 ± 0.001	8.50 ± 1.66	74 ± 36	60 ± 6
ED_{10}	−0.447 ± 0.286	0.62 ± 0.60	82 ± 5	59 ± 28
ED_{30}	−0.557 ± 0.060	0.53 ± 0.10	62 ± 14	119 ± 67
ED_{60}	−0.447 ± 0.119	0.72 ± 0.06	137 ± 27	112 ± 46
ED_{120}	−0.356 ± 0.030	0.27 ± 0.06	302 ± 232	60 ± 8
ED_{300}	−0.362 ± 0.030	0.07 ± 0.01	137 ± 23	89 ± 10

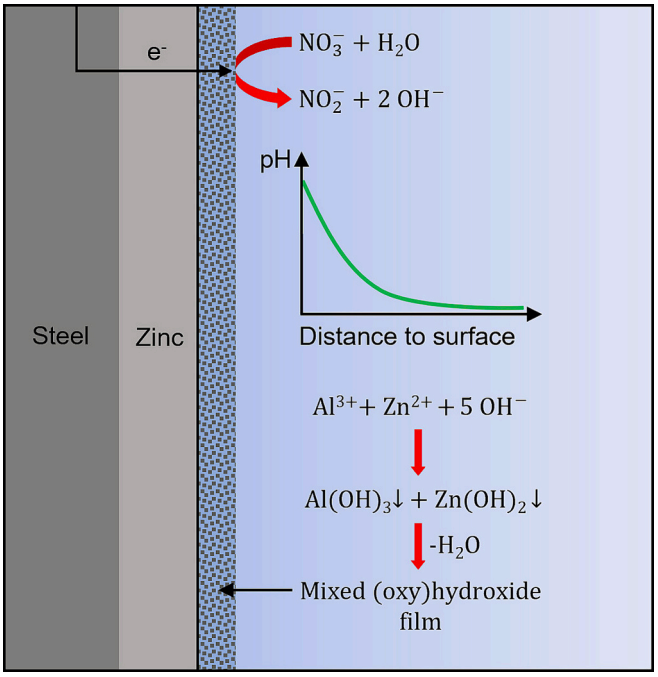

Fig. 11. Scheme of the mixed (oxy)hydroxide film deposition by precipitation and transformation mechanism. The deposition is promoted by the rise in pH at the electrolyte/zinc interface.

$$Al^{3+} + 3\,OH^- \rightarrow AlOOH + H_2O \quad (4)$$

Even though the Zn:Al ratio in the solution was 5:2, XPS measurements showed that the resulting layer is enriched with aluminium, which could be caused by the precipitation of aluminium hydroxide at a lower pH compared to zinc hydroxide [19,22]. In a second step, the mixed hydroxides could transform to a mixed metal oxide film via

dehydration reactions [61–63].

$$Zn(OH)_2 \rightarrow ZnO + H_2O \quad (5)$$

$$Al(OH)_3 \rightarrow AlOOH + H_2O \quad (6)$$

$$2\ AlOOH \rightarrow Al_2O_3 + H_2O \quad (7)$$

Additionally, zinc aluminate could be deposited in sufficiently alkaline conditions [64].

$$2\left[Al(OH)_4\right]^- + Zn^{2+} \rightarrow ZnAl_2O_4 + 4\ H_2O \quad (8)$$

However, the resulting films were not artificially dehydrated and still contain (oxy)hydroxides, resulting in an amorphous mixed layer. The findings are consistent with the investigations of Tseng et al. reporting the formation of an amorphous phase in very similar conditions, which they interpreted as a polynuclear hydroxo-complex [17]. The time dependence of the composition observed in the FT-IRRAS measurement of ED_{300} may be a result of the decreasing concentration of aluminium at the interface wherefore more zinc hydroxide is deposited.

The formed films lead to an effective inhibition of corrosion reactions in chloride containing electrolytes as shown by the electrochemical analysis. Both the anodic reactions as well as the cathodic reactions are slowed down as the film thickness increases.

5. Conclusion

Cathodic electrodeposition of corrosion resistant mixed zinc/aluminium hydroxide films on zinc coated steel was achieved within short deposition times from aqueous electrolyte containing aluminium and zinc nitrate. FE-SEM cross sectional analysis showed that the deposited layers had a maximum layer thickness of about 200 nm after 300 s deposition.

The spectroscopic analysis of the film composition revealed that aluminium and zinc hydroxides are deposited at first, which subsequently can transform to aluminium oxyhydroxide, aluminium oxide and zinc oxide via dehydration reactions. As the deposition of aluminium hydroxide is faster than the deposition of zinc hydroxide, the resulting films are enriched with aluminium hydroxide resulting in an Al:Zn ratio of about 4:1 as shown by XPS. XRD and FIB-SEM studies revealed that the formed films are predominantly amorphous and contain nanopores. Moreover, we assume that the incorporated zinc oxide is responsible for the electronic conductivity of the films.

The deposited mixed layers provide efficient barrier properties even at 24 h of corrosive exposure in chloride containing aqueous electrolytes, as measured by means of EIS. The inhibition of corrosion reactions by the deposited thin films was also confirmed by linear sweep voltammetry, showing an anodic shift of the corrosion potential and corrosion current density which is decreased by two orders of magnitude compared to the uncoated substrate.

Deposited films already provide an inhibiting effect at thickness values of few nanometers corresponding to a deposition time of about 10 s. This property could promote the application of this thin film deposition process for technical applications which require short cycle times.

CRediT authorship contribution statement

Chen-Ni Liu: Writing – original draft, Visualization, Methodology, Investigation. **Lukas Ruhm:** Writing – original draft, Visualization, Validation, Investigation, Formal analysis. **Marten Huck:** Writing – original draft, Investigation, Formal analysis. **Hans-Georg Steinrück:** Writing – original draft, Supervision, Resources, Formal analysis. **Philipp Wagener:** Writing – original draft, Resources, Funding acquisition, Conceptualization. **Marcel Roth:** Writing – original draft, Supervision, Formal analysis, Conceptualization. **Ingo Klüppel:** Writing – original draft, Visualization, Investigation. **Guido Grundmeier:** Writing – original draft, Supervision, Resources, Funding acquisition, Conceptualization.

Declaration of competing interest

The authors declare that they have no known competing financial interests or personal relationships that could have appeared to influence the work reported in this paper.

Acknowledgement

The authors gratefully acknowledge the financial support of European Regional Development Fund (ERDF- or *EFRE* in German) within OP EFRE NRW of the project "Strukturierte Zink(oxid)schichten", EFRE-0800644, (C.-N. Liu, L. Ruhm, G. Grundmeier), EFRE-0800673 (P. Wagener), and EFRE-0800654 (M. Roth, I. Klüppel). M. Huck and H.G. Steinrück acknowledge the funding by the German Federal Ministry of Research, Technology and Space (BMFTR) and the Ministry of Economic Affairs, Industry, Climate Action and Energy of the State of North Rhine-Westphalia through the project HC–H2, and from German Federal Ministry of Research, Technology and Space (BMFTR) via Project 05K22PP1 and 05K24CJ1.

Appendix A. Supplementary data

Supplementary data to this article can be found online at https://doi.org/10.1016/j.surfcoat.2025.133044.

Data availability

XRD raw data and some plots are provided on Zenodo (doi.org/10.5281/zenodo.15591123).

References

[1] Z. Yu, J. Hu, H. Meng, A review of recent developments in coating systems for hot-dip galvanized steel, Front. Mater. 7 (2020) 74, https://doi.org/10.3389/fmats.2020.00074.
[2] A.-M. Lazar, W.P. Yespica, S. Marcelin, N. Pébère, D. Samélor, C. Tendero, C. Vahlas, Corrosion protection of 304L stainless steel by chemical vapor deposited alumina coatings, Corros. Sci. 81 (2014) 125–131, https://doi.org/10.1016/j.corsci.2013.12.012.
[3] D.G. Altenpohl, Use of boehmite films for corrosion protection of aluminum, Corrosion 18 (1962) 143t–153t, https://doi.org/10.5006/0010-9312-18.4.143.
[4] Q.-Q. He, M.-J. Zhou, J.-M. Hu, Electrodeposited Zn-Al layered double hydroxide films for corrosion protection of aluminum alloys, Electrochim. Acta 355 (2020) 136796, https://doi.org/10.1016/j.electacta.2020.136796.
[5] X. Guo, S. Xu, L. Zhao, W. Lu, F. Zhang, D.G. Evans, X. Duan, One-step hydrothermal crystallization of a layered double hydroxide/alumina bilayer film on aluminum and its corrosion resistance properties, Langmuir 25 (2009) 9894–9897, https://doi.org/10.1021/la901012w.
[6] M.A. Iqbal, L. Sun, A.T. Barrett, M. Fedel, Layered double hydroxide protective films developed on aluminum and aluminum alloys: synthetic methods and anti-corrosion mechanisms, Coatings 10 (2020) 428, https://doi.org/10.3390/coatings10040428.
[7] M.V. Bukhtiyarova, A review on effect of synthesis conditions on the formation of layered double hydroxides, J. Solid State Chem. 269 (2019) 494–506, https://doi.org/10.1016/j.jssc.2018.10.018.
[8] H. Konno, K. Narumi, H. Habazaki, Molybdate/Al(III) composite films on steel and zinc-plated steel by chemical conversion, Corros. Sci. 44 (2002) 1889–1900, https://doi.org/10.1016/S0010-938X(01)00174-3.
[9] G. Wu, X. Zeng, G. Yuan, Growth and corrosion of aluminum PVD-coating on AZ31 magnesium alloy, Mater. Lett. 62 (2008) 4325–4327, https://doi.org/10.1016/j.matlet.2008.07.014.
[10] K. Bobzin, E. Lugscheider, M. Maes, P. Immich, Alumina PVD tool coatings for the use in semi solid metal forming of steel, SSP 116-117 (2006) 704–707, https://doi.org/10.4028/www.scientific.net/SSP.116-117.704.
[11] A. Schütze, D.T. Quinto, Pulsed plasma-assisted PVD sputter-deposited alumina thin films, Surf. Coat. Technol. 162 (2003) 174–182, https://doi.org/10.1016/S0257-8972(02)00705-3.
[12] D. Hochauer, C. Mitterer, M. Penoy, C. Michotte, H.P. Martinz, M. Kathrein, Titanium doped CVD alumina coatings, Surf. Coat. Technol. 203 (2008) 350–356, https://doi.org/10.1016/j.surfcoat.2008.09.015.

[13] A. Zanurin, N.A. Johari, J. Alias, H. Mas Ayu, N. Redzuan, S. Izman, Research progress of sol-gel ceramic coating: a review, Mater. Today Proc. 48 (2022) 1849–1854, https://doi.org/10.1016/j.matpr.2021.09.203.
[14] X. Lu, R. Zhu, Y. He, Electrodeposited thin oxide films, Surf. Coat. Technol. 79 (1996) 19–24, https://doi.org/10.1016/0257-8972(95)02456-5.
[15] A.M. Abdel Haleem, M. Ichimura, Electrochemical deposition of aluminum oxide thin films from aqueous baths, Mater. Lett. 130 (2014) 26–28, https://doi.org/10.1016/j.matlet.2014.05.061.
[16] J.D. Watkins, H. Nulwala, S. Brankovic, Electrochemical deposition of aluminum-based coatings from aqueous systems. https://www.osti.gov/biblio/1598787, 2020.
[17] Y.T. Tseng, A. Choudhury, K.C. Peng, J.H. Chen, C.T. Chou, J.C. Lin, Concentration effect of aluminum nitrate on the crystalline−amorphous transition between Al-doped ZnO nanorods and nanostructures prepared by electrochemical deposition, Electrochim. Acta 308 (2019) 350–362, https://doi.org/10.1016/j.electacta.2019.04.006.
[18] O. Baka, A. Azizi, S. Velumani, G. Schmerber, A. Dinia, Effect of Al concentrations on the electrodeposition and properties of transparent Al-doped ZnO thin films, J. Mater. Sci. Mater. Electron. 25 (2014) 1761–1769, https://doi.org/10.1007/s10854-014-1796-3.
[19] I. Gualandi, M. Monti, E. Scavetta, D. Tonelli, V. Prevot, C. Mousty, Electrodeposition of layered double hydroxides on platinum: insights into the reactions sequence, Electrochim. Acta 152 (2015) 75–83, https://doi.org/10.1016/j.electacta.2014.11.096.
[20] M.S. Yarger, E.M.P. Steinmiller, K.-S. Choi, Electrochemical synthesis of Zn-Al layered double hydroxide (LDH) films, Inorg. Chem. 47 (2008) 5859–5865, https://doi.org/10.1021/ic800193j.
[21] S. Otani, J. Katayama, H. Umemoto, M. Matsuoka, Effect of Bath temperature on the electrodeposition mechanism of zinc oxide film from zinc nitrate solution, J. Electrochem. Soc. 153 (2006) C551, https://doi.org/10.1149/1.2205187.
[22] A. Packter, A. Derry, The Coprecipitation of zinc Aluminium hydroxide powders from aqueous solution with sodium hydroxide: precipitate compositions and Coprecipitation mechanisms, Cryst. Res. Technol. 21 (1986) 1281–1286, https://doi.org/10.1002/crat.2170211008.
[23] S. Amanian, R. Naderi, M. Mahdavian, The role of an in-situ grown Zn-Al layered double hydroxide conversion coating in the protective properties of epoxy coating on galvanized steel, J. Electrochem. Soc. 169 (2022) 31511, https://doi.org/10.1149/1945-7111/ac5d95.
[24] T. Thi Xuan Hang, T.T. Pham, T.D. Nguyen, M.-G. Olivier, A review: Hydrotalcite layers as protective coatings on zinc and zinc alloys, Vietnam J. Sci. Technol. 62 (2024) 1047–1064, https://doi.org/10.15625/2525-2518/21045.
[25] K.A. Yasakau, A. Kuznetsova, H.M. Maltanava, S.K. Poznyak, M. Ferreira, M. L. Zheludkevich, Corrosion protection of zinc by LDH conversion coatings, Corros. Sci. 229 (2024) 111889, https://doi.org/10.1016/j.corsci.2024.111889.
[26] T. Xu, L. Yu, J.-M. Hu, In-situ Zn-Al layered double hydroxide conversion coatings prepared on galvanized steels by a two-step electrochemical method, Corros. Sci. 233 (2024) 112057, https://doi.org/10.1016/j.corsci.2024.112057.
[27] N. Murer, N.A. Missert, R.G. Buchheit, Finite element modeling of the galvanic corrosion of aluminum at engineered copper particles, J. Electrochem. Soc. 159 (2012) C265–C276, https://doi.org/10.1149/2.102206jes.
[28] X.-D. Gao, F. Peng, X.-M. Li, W.-D. Yu, J.-J. Qiu, Growth of highly oriented ZnO films by the two-step electrodeposition technique, J. Mater. Sci. 42 (2007) 9638–9644, https://doi.org/10.1007/s10853-007-1970-6.
[29] R. Salazar, C. Lévy-Clément, V. Ivanova, Galvanostatic deposition of ZnO thin films, Electrochim. Acta 78 (2012) 547–556, https://doi.org/10.1016/j.electacta.2012.06.070.
[30] T. Yoshida, D. Komatsu, N. Shimokawa, H. Minoura, Mechanism of cathodic electrodeposition of zinc oxide thin films from aqueous zinc nitrate baths, Thin Solid Films 451-452 (2004) 166–169, https://doi.org/10.1016/j.tsf.2003.10.097.
[31] M. Stumpp, T. Nguyen, C. Lupo, D. Schlettwein, Interplay of different reaction pathways in the pulsed Galvanostatic deposition of zinc oxide, Electrochim. Acta 169 (2015) 367–375, https://doi.org/10.1016/j.electacta.2015.04.038.
[32] R. Grothe, J. Striewe, D. Meinderink, T. Tröster, G. Grundmeier, Enhanced corrosion resistance of adhesive/galvanised steel interfaces by nanocrystalline ZnO thin film deposition and molecular adhesion promoting films, J. Adhes. 98 (2022) 2210–2230, https://doi.org/10.1080/00218464.2021.1957676.
[33] M. Izaki, T. Omi, Electrolyte optimization for cathodic growth of zinc oxide films, J. Electrochem. Soc. 143 (1996) L53–L55, https://doi.org/10.1149/1.1836529.
[34] D. Meinderink, C. Kielar, O. Sobol, L. Ruhm, F. Rieker, K. Nolkemper, A.G. Orive, O. Ozcan, G. Grundmeier, Effect of PAA-induced surface etching on the adhesion properties of ZnO nanostructured films, Int. J. Adhes. Adhes. 106 (2021) 102812, https://doi.org/10.1016/j.ijadhadh.2021.102812.
[35] S. Xu, Z.L. Wang, One-dimensional ZnO nanostructures: solution growth and functional properties, Nano Res. 4 (2011) 1013–1098, https://doi.org/10.1007/s12274-011-0160-7.
[36] A.-L. Goff, S. Joiret, B. Saïdani, R. Wiart, In-situ Raman spectroscopy applied to the study of the deposition and passivation of zinc in alkaline electrolytes, J. Electroanal. Chem. Interfacial Electrochem. 263 (1989) 127–135, https://doi.org/10.1016/0022-0728(89)80129-9.
[37] V. Russo, M. Ghidelli, P. Gondoni, C.S. Casari, A. Li Bassi, Multi-wavelength Raman scattering of nanostructured Al-doped zinc oxide, J. Appl. Phys. 115 (2014) 073508, https://doi.org/10.1063/1.4866322.
[38] D. Caffrey, A. Zhussupbekova, R.K. Vijayaraghavan, A. Ainabayev, A. Kaisha, G. Sugurbekova, I.V. Shvets, K. Fleischer, Crystallographic characterisation of ultra-thin, or amorphous transparent conducting oxides-the case for Raman spectroscopy, Materials 13 (2020) 267, https://doi.org/10.3390/ma13020267.
[39] L.B. Staal, S.S. Charan Pushparaj, C. Forano, V. Prevot, D.B. Ravnsbæk, M. Bjerring, U.G. Nielsen, Competitive reactions during synthesis of zinc aluminum layered double hydroxides by thermal hydrolysis of urea, J. Mater. Chem. A 5 (2017) 21795–21806, https://doi.org/10.1039/C7TA05761J.
[40] E.M. Seftel, R.G. Ciocarlan, B. Michielsen, V. Meynen, S. Mullens, P. Cool, Insights into phosphate adsorption behavior on structurally modified ZnAl layered double hydroxides, Appl. Clay Sci. 165 (2018) 234–246, https://doi.org/10.1016/j.clay.2018.08.018.
[41] L. Guo, F. Zhang, J.-C. Lu, R.-C. Zeng, S.-Q. Li, L. Song, J.-M. Zeng, A comparison of corrosion inhibition of magnesium aluminum and zinc aluminum vanadate intercalated layered double hydroxides on magnesium alloys, Front. Mater. Sci. 12 (2018) 198–206, https://doi.org/10.1007/s11706-018-0415-2.
[42] D. Persson, D. Thierry, N. LeBozec, T. Prosek, In situ infrared reflection spectroscopy studies of the initial atmospheric corrosion of Zn–Al–Mg coated steel, Corros. Sci. 72 (2013) 54–63, https://doi.org/10.1016/j.corsci.2013.03.005.
[43] J. van den Brand, O. Blajiev, P.C.J. Beentjes, H. Terryn, J.H.W. de Wit, Interaction of anhydride and carboxylic acid compounds with aluminum oxide surfaces studied using infrared reflection absorption spectroscopy, Langmuir 20 (2004) 6308–6317, https://doi.org/10.1021/la0496845.
[44] P.R. Underhill, A.N. Rider, Hydrated oxide film growth on aluminium alloys immersed in warm water, Surf. Coat. Technol. 192 (2005) 199–207, https://doi.org/10.1016/j.surfcoat.2004.10.011.
[45] J. Winiarski, W. Tylus, K. Winiarska, I. Szczygieł, B. Szczygieł, XPS and FT-IR characterization of selected synthetic corrosion products of zinc expected in neutral environment containing chloride ions, J. Spectrosc. 2018 (2018) 1–14, https://doi.org/10.1155/2018/2079278.
[46] J.T. Kloprogge, D. Wharton, L. Hickey, R.L. Frost, Infrared and Raman study of interlayer anions CO 32− NO 3− SO 42− and ClO 4− in Mg/Al-hydrotalcite, Am. Mineral. 87 (2002) 623–629, https://doi.org/10.2138/am-2002-5-604.
[47] N.J. Nicholas, G.V. Franks, W.A. Ducker, The mechanism for hydrothermal growth of zinc oxide, CrystEngComm 14 (2012) 1232–1240, https://doi.org/10.1039/C1CE06039B.
[48] R.L. Frost, J.T. Kloprogge, S.C. Russell, J.L. Szetu, Vibrational spectroscopy and Dehydroxylation of aluminum (Oxo)hydroxides: gibbsite, Appl. Spectrosc. 53 (1999) 423–434, https://doi.org/10.1366/0003702991946884.
[49] M.R. Alexander, S. Payan, T.M. Duc, Interfacial interactions of plasma-polymerized acrylic acid and an oxidized aluminium surface investigated using XPS, FTIR and poly(acrylic acid) as a model compound, Surf. Interface Anal. 26 (1998) 961–973, https://doi.org/10.1002/(SICI)1096-9918(199812)26:13<961:AID-SIA432>3.0.CO;2-7.
[50] M.C. Hales, R.L. Frost, Synthesis and vibrational spectroscopic characterisation of synthetic hydrozincite and smithsonite, Polyhedron 26 (2007) 4955–4962, https://doi.org/10.1016/j.poly.2007.07.002.
[51] B.P. Payne, M.C. Biesinger, N.S. McIntyre, X-ray photoelectron spectroscopy studies of reactions on chromium metal and chromium oxide surfaces, J. Electron Spectrosc. Relat. Phenom. 184 (2011) 29–37, https://doi.org/10.1016/j.elspec.2010.12.001.
[52] M.C. Biesinger, L.W. Lau, A.R. Gerson, R.S. Smart, Resolving surface chemical states in XPS analysis of first row transition metals, oxides and hydroxides: Sc, Ti, V, cu and Zn, Appl. Surf. Sci. 257 (2010) 887–898, https://doi.org/10.1016/j.apsusc.2010.07.086.
[53] E. Diler, B. Lescop, S. Rioual, G. Nguyen Vien, D. Thierry, B. Rouvellou, Initial formation of corrosion products on pure zinc and MgZn2 examinated by XPS, Corros. Sci. 79 (2014) 83–88, https://doi.org/10.1016/j.corsci.2013.10.029.
[54] J. Duchoslav, R. Steinberger, M. Arndt, D. Stifter, XPS study of zinc hydroxide as a potential corrosion product of zinc: rapid X-ray induced conversion into zinc oxide, Corros. Sci. 82 (2014) 356–361, https://doi.org/10.1016/j.corsci.2014.01.037.
[55] J. van den Brand, P.C. Snijders, W.G. Sloof, H. Terryn, J.H.W. de Wit, Acid−base characterization of aluminum oxide surfaces with XPS, J. Phys. Chem. B 108 (2004) 6017–6024, https://doi.org/10.1021/jp037877f.
[56] J.T. Kloprogge, L.V. Duong, B.J. Wood, R.L. Frost, XPS study of the major minerals in bauxite: gibbsite, bayerite and (pseudo-)boehmite, J. Colloid Interface Sci. 296 (2006) 572–576, https://doi.org/10.1016/j.jcis.2005.09.054.
[57] J. Zuo, A. Erbe, Optical and electronic properties of native zinc oxide films on polycrystalline Zn, Phys. Chem. Chem. Phys. 12 (2010) 11467–11476, https://doi.org/10.1039/c004532b.
[58] S.W. Gaarenstroom, N. Winograd, Initial and final state effects in the ESCA spectra of cadmium and silver oxides, J. Chem. Phys. 67 (1977) 3500–3506, https://doi.org/10.1063/1.435347.
[59] R.K. Hart, A study of boehmite formation on aluminium surfaces by electron diffraction, Trans. Faraday Soc. 50 (1954) 269, https://doi.org/10.1039/TF9545000269.
[60] X. Du, Y. Wang, X. Su, J. Li, Influences of pH value on the microstructure and phase transformation of aluminum hydroxide, Powder Technol. 192 (2009) 40–46, https://doi.org/10.1016/j.powtec.2008.11.008.
[61] N. Jraba, H. Tounsi, T. Makhlouf, Valorization of aluminum chips into γ-Al2O3 and η-Al2O3 with high surface areas via the precipitation route, Waste Biomass Valoriz. 9 (2018) 1003–1014, https://doi.org/10.1007/s12649-016-9786-8.
[62] S. Jiao, K. Zhang, S. Bai, H. Li, S. Gao, H. Li, J. Wang, Q. Yu, F. Guo, L. Zhao, Controlled morphology evolution of ZnO nanostructures in the electrochemical

deposition: from the point of view of chloride ions, Electrochim. Acta 111 (2013) 64–70, https://doi.org/10.1016/j.electacta.2013.08.050.
[63] T. Sato, Thermal decomposition of aluminium hydroxides to aluminas, Thermochim. Acta 88 (1985) 69–84, https://doi.org/10.1016/0040-6031(85)85415-0.
[64] I. Miron, C. Enache, M. Vasile, I. Grozescu, Optical properties of ZnAl 2 O 4 nanomaterials obtained by the hydrothermal method, Phys. Scr. T149 (2012) 14064, https://doi.org/10.1088/0031-8949/2012/T149/014064.